

# Imaging emergent heavy Dirac fermions of a topological Kondo insulator

Harris Pirie<sup>1</sup>, Yu Liu<sup>1</sup>, Anjan Soumyanarayanan<sup>1,6</sup>, Pengcheng Chen<sup>1</sup>, Yang He<sup>1</sup>, M. M. Yee<sup>1</sup>, P. F. S. Rosa<sup>2</sup>, J. D. Thompson<sup>2</sup>, Dae-Jeong Kim<sup>3</sup>, Z. Fisk<sup>3</sup>, Xiangfeng Wang<sup>4</sup>, Johnpierre Paglione<sup>4</sup>, Dirk K. Morr<sup>5</sup>, M. H. Hamidian<sup>1\*</sup> and Jennifer E. Hoffman<sup>1\*</sup>

**The interplay between strong electron interactions and band topology is a new frontier in the search for exotic quantum phases. The Kondo insulator  $\text{SmB}_6$  has emerged as a promising platform because its correlation-driven bulk gap is predicted to host topological surface modes entangled with  $f$  electrons, spawning heavy Dirac fermions<sup>1–4</sup>. Unlike the conventional surface states of non-interacting topological insulators, heavy Dirac fermions are expected to harbour spontaneously generated quantum anomalous Hall states<sup>5</sup>, non-Abelian quantum statistics<sup>6,7</sup>, fractionalization<sup>8</sup> and topological order<sup>6–8</sup>. However, the small energy scales required to probe heavy Dirac fermions have complicated their experimental realization. Here we use high-energy-resolution spectroscopic imaging in real and momentum space on  $\text{SmB}_6$ . On cooling below 35 K, we observe the opening of an insulating gap that expands to 14 meV at 2 K. Within the gap, we image the formation of linearly dispersing surface states with effective masses reaching  $410 \pm 20 m_e$  (where  $m_e$  is the mass of the electron). Our results demonstrate the presence of correlation-driven heavy surface states in  $\text{SmB}_6$ , in agreement with theoretical predictions<sup>1–4</sup>. Their high effective mass translates to a large density of states near zero energy, which magnifies their susceptibility to the anticipated novel orders and their potential utility.**

Kondo insulators (KIs) are formed when strong interactions within a periodic array of localized moments, usually  $f$  electrons, lead to reorganization of the low-temperature electronic structure<sup>9</sup>. This process opens an insulating gap  $\Delta$ , driven by hybridization between renormalized, low-lying localized states and itinerant conduction electrons (Fig. 1a,b). The KI  $\text{SmB}_6$ , in which localized  $f$  and itinerant  $d$  states are contributed by Sm atoms (Fig. 1a inset), exhibits such a characteristic metal–insulator crossover at temperature  $T_{\text{MI}} \approx 30\text{--}50\text{ K}$  (refs. 10,11). Mysteriously, the resistance plateaus below  $5\text{ K}$ <sup>10,11</sup>, signalling the onset of a new conduction channel whose origin has been intensely debated for decades<sup>9</sup>. One resolution of this long-standing problem posits that  $\text{SmB}_6$  hosts a novel topological KI (TKI) ground state<sup>1–4</sup>, whose low-temperature conductivity originates from topologically emergent Dirac surface states within the narrow energy window of the KI gap. Large  $f$ -electron contributions to these states are predicted to yield the heaviest Dirac states of any known material.

Electronic structure calculations predict  $\text{SmB}_6$  to be a TKI<sup>2–4</sup>. The expected bulk band structure of the associated Kondo lattice model

contains two crystal-field-split  $f$  states and a band of  $d$  electrons (Fig. 1a,b). Quantum mechanical mixing between opposite parity  $f$  and  $d$  states vanishes at the momentum-space high-symmetry points  $\mathbf{k}^* = \Gamma, X, M, R$  where parity is a good quantum number, thus forcing nodes in the hybridization parameter,  $V(\mathbf{k})$ , such that  $\langle f|V(\mathbf{k}^*)|d\rangle = 0$  (Fig. 1c). Consequently, the parity  $\delta(\mathbf{k})$  of the fully hybridized filled states is inverted at three symmetry-equivalent X points in the three-dimensional (3D) cubic Brillouin zone. The resulting topological invariant predicts a non-trivial topological phase<sup>1,2</sup>, captured by the index  $\nu = \delta_{\Gamma} \delta_X (\delta_X \delta_M)^3 = -1$ , where  $\delta_{\Gamma, X, M, R} = \pm 1$  is the parity of filled bands at high-symmetry points (red circles in Fig. 1d). On the  $\text{SmB}_6$  Kondo lattice, topologically emergent surface states are predicted to (1) lie predominantly within the energy interval of the correlation-driven bulk gap, (2) have a Dirac spectrum, (3) be centred at the  $\bar{\Gamma}$  and two  $\bar{X}$  points of the two-dimensional (2D) surface Brillouin zone, and (4) have distinct band velocities. The last prediction follows intuitively from observing that 3D constant-energy manifolds at the X points with different relative orientations create inequivalent 2D projections (Fig. 1d). Consequently, surface states connecting 2D-projected bulk hybridized bands are expected to have distinct velocities at the  $\bar{\Gamma}$  and  $\bar{X}$  points (Fig. 1d).

Experimentally, temperature-dependent point-contact spectroscopy<sup>12</sup> has shown the  $\text{SmB}_6$  bulk electronic structure to be consistent with a KI, while surface conduction channels have been demonstrated by geometry-dependent transport measurements at low temperatures<sup>11,13</sup>. Magnetothermoelectric studies<sup>14</sup> imply that the (110) surface of  $\text{SmB}_6$  may harbour heavy metallic surface states, although their topological nature is not clear. Torque magnetometry experiments<sup>15</sup> on the (110) surface measured surface states whose velocities are more than two orders of magnitude larger than expected<sup>4</sup>. In contrast, a separate quantum oscillation measurement attributed these states to the bulk<sup>16</sup>. Direct energy- and momentum-resolved electronic structure mapping by angle-resolved photoemission spectroscopy (ARPES)<sup>17–19</sup> appeared to show linearly dispersing surface bands with velocities at least an order of magnitude larger than those expected for the Dirac fermions of  $\text{SmB}_6$  and with an inferred Dirac point buried far below the bulk gap<sup>4</sup> (Supplementary Table 2). Because much of the active physics in the ground state resides within a small energy window set by the KI gap— $\Delta \approx 8\text{--}10\text{ meV}$ , as revealed by transport experiments<sup>13,20</sup>—ARPES mapping of the electronic structure is limited when it comes to detecting narrow bandwidth states of an incipient TKI<sup>21</sup>. Furthermore, ARPES measurements typically average over

<sup>1</sup>Department of Physics, Harvard University, Cambridge, MA, USA. <sup>2</sup>Los Alamos National Laboratory, Los Alamos, NM, USA. <sup>3</sup>Department of Physics and Astronomy, University of California at Irvine, Irvine, CA, USA. <sup>4</sup>Center for Nanophysics and Advanced Materials, Department of Physics, University of Maryland, College Park, MD, USA. <sup>5</sup>Department of Physics, University of Illinois at Chicago, Chicago, IL, USA. <sup>6</sup>Present address: Institute of Materials Research and Engineering, Agency for Science, Technology and Research, Singapore, Singapore. \*e-mail: [m.hamidian@gmail.com](mailto:m.hamidian@gmail.com); [jhoffman@physics.harvard.edu](mailto:jhoffman@physics.harvard.edu)

different (polar) surface terminations with relative intensity and chemical potential shifts in their surface states, rendering interpretations difficult<sup>22,23</sup>. Collectively, these suggestive but controversial experiments have renewed the urgency of discovering topological states arising from strong electronic interactions. Ultimately, observation of strongly correlated topological states in  $\text{SmB}_6$  requires measurements on a uniform and ordered surface termination, access to filled and empty states at low temperatures, and meV energy resolution in momentum space to disentangle the shallow dispersions of a bulk KI band structure (Fig. 1b) and surface heavy Dirac fermions (Fig. 1d).

Here we use spectroscopic scanning tunnelling microscopy (STM) to directly map the structure and formation of heavy Dirac states on the (001) surface of  $\text{SmB}_6$  in two complementary measurements. First, we resolve the energy ( $E$ ) and momentum-space ( $\mathbf{k}$ ) structure of two inequivalent Dirac cones from quasiparticle interference (QPI) patterns around atomic defects by measuring spatially resolved differential conductance,  $g(\mathbf{r}, E) \equiv dI/dV(\mathbf{r}, E = eV)$ , where  $I$  is the STM tunnelling current,  $V$  is the applied bias,  $\mathbf{r}$  is the tip position and  $e$  is the electron charge. Second, we track the formation of heavy Dirac states from their additional contributions to the low-temperature tunnelling spectroscopy by measuring  $g(E, T)$ . We find that their onset is far more abrupt than expected from thermal broadening; instead, it is correlated with the development of the bulk KI. Our measurements corroborate one another by each detecting a consistent Dirac-point energy of  $E_D \approx -5$  meV.

We studied nominally pure, 0.1% Gd-doped and 0.5% Fe-doped  $\text{SmB}_6$  by cleaving single crystals in a cryogenic ultrahigh vacuum and directly inserting into the STM at 4K (see Methods and Supplementary Section I). We found that adding a small amount of Gd or Fe dopants enhanced quasiparticle scattering, but our observed QPI dispersions were consistent across all samples. We focused on regions where exactly half of the atoms remain on the cleaved surface, resulting in an ordered  $(2 \times 1)$  reconstruction (Fig. 2a)<sup>24,25</sup>. We identify this surface as a half-Sm termination because intentional Fe dopants, which substitute for Sm, appeared at the lattice sites. A half-Sm termination is beneficial because it is non-polar, eliminating the possibility of polarity-driven surface states<sup>26</sup>. Furthermore, the  $(2 \times 1)$  reconstruction increases our sensitivity to one of the  $\bar{X}$ -point Dirac cones by folding it to the  $\bar{\Gamma}$  point (Fig. 2b), where it has a longer vacuum decay length due to its lower in-plane momentum<sup>27</sup>.

We detected clear interference patterns in raw  $g(\mathbf{r}, E)$  around defects, caused by the elastic scattering of quasiparticles, as shown in Fig. 2c,d. Their energy-dependent wavevector,  $\mathbf{q}(E) = \mathbf{k}_f(E) - \mathbf{k}_i(E)$ , encodes the momentum transfer between initial ( $\mathbf{k}_i$ ) and final ( $\mathbf{k}_f$ ) states and tracks the underlying electronic structure<sup>28–30</sup>. In  $\text{SmB}_6$ , QPI patterns are typically short-ranged around defects, as in Fig. 2d, reflecting contributions from localized  $f$  electrons. Correspondingly, they manifest as fairly broad peaks in the magnitude of the Fourier-transformed differential conductance,  $|\tilde{g}(\mathbf{q}, E)|$ , with the highest signal to noise ratio along the  $q_y$  direction (Fig. 2e), primarily due to the anisotropy of the scattering form factor (see Supplementary Section V). We quantified their wavevector by fitting angle-averaged linecuts of  $|\tilde{g}(\mathbf{q}, E)|$  along  $q_y$  with a set of Gaussians (Fig. 2f, details in Supplementary Section IV). The QPI wavevector changes rapidly with energy, as shown in Fig. 3, but can be broadly divided into two energy ranges. For energies within the KI gap  $\Delta$ , there are two sets of roughly linear dispersions: one very shallow (green guides in Fig. 3), and one steep (blue guides). For energies outside this range, the set of dispersions can be mapped to the known low-energy KI states of  $\text{SmB}_6$  (details in Supplementary Section VIII). None of these dispersions were noticeably affected by magnetic fields up to 9T (Fig. 3a,b), consistent with previous STM spectra<sup>31</sup> (see Supplementary Section VI). All dispersions were reproducible in six different raw datasets on three distinct samples from two different growers, with distinct STM acquisition parameters, three of which are shown in Fig. 3.

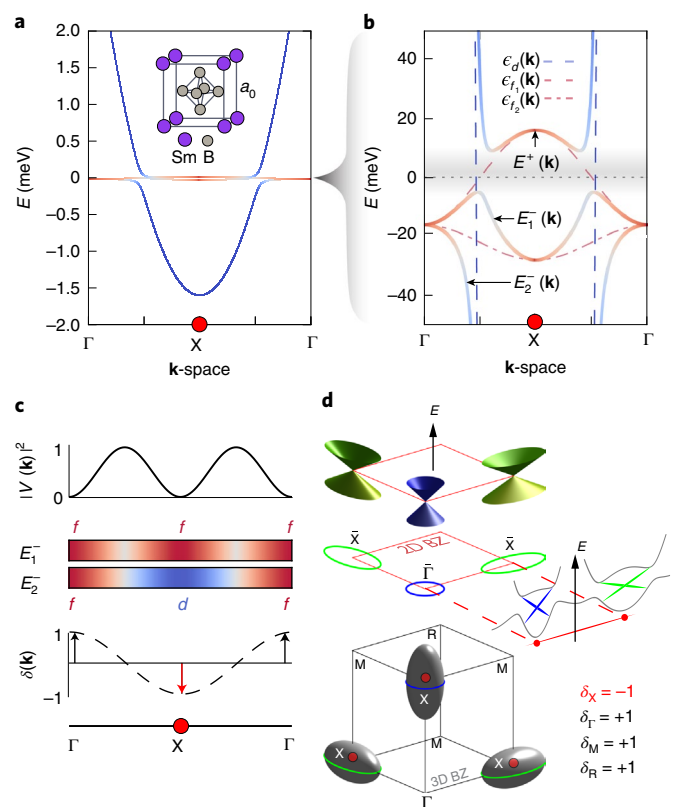


**Fig. 1 | Anticipated topological Kondo insulator electronic structure of  $\text{SmB}_6$ .**

**a**, The KI electronic structure consists of an itinerant  $d$ -character band (blue), centred around the X point, which hybridizes with localized  $f$ -character (red) states. Both  $f$  and  $d$  states are contributed by the Sm atoms, which form a cubic unit cell with lattice constant  $a_0$  (inset). **b**, Narrow energy window of the same electronic structure in **a**. At low temperatures a  $d$  band ( $\epsilon_d$ ) and two closely spaced crystal-field-split  $f$  states ( $\epsilon_{f1}, \epsilon_{f2}$ ) hybridize to form three separate bands ( $E^+, E_1^-, E_2^-$ ) with a gap of several millielectronvolts. **c**, The topological invariant for the KI electronic structure is calculated from a product of parity eigenvalues, which are opposite for  $d$  and  $f$  states. Top: nodes in the hybridization parameter,  $|V(\mathbf{k})|^2$ , at the X and  $\Gamma$  points lead to pure  $f$  or  $d$  character of the hybridized bands at those locations. Middle: the filled bands,  $E_1^-, E_2^-$  have full  $f$  character at  $\Gamma$  and evolve to either  $d$  or  $f$  at X. Bottom: thus, total parity,  $\delta$ , is reversed only at the X points (marked red circle). **d**, The cubic TKI electronic structure has parity inversion at three X points (red balls) in the 3D Brillouin zone (BZ) giving a  $Z_2$  topological index  $\nu = \delta_{\bar{\Gamma}} \delta_{\bar{X}} (\delta_{\bar{X}} \delta_{\bar{X}})^3 = -1$  that encodes the strong topological state. When projected onto the 2D BZ, the inversion manifests at the  $\bar{\Gamma}$  and two  $\bar{X}$  points (red circles) and consequently sets the locations of the predicted 2D Dirac states. These Dirac surface states acquire different velocities from the inequivalent projections of the bulk elliptical constant-energy contours onto the 2D surface BZ (green ellipses and blue circle).

The in-gap states we image are in excellent agreement with expectations for a TKI phase with  $f$ -dominated heavy Dirac fermions<sup>2–4</sup>. Their dispersions, overlaid on Fig. 3a,c, match the two sets of linear traces expected from scattering within distinct Dirac cones, (labelled  $q_1$  and  $q_2$  in Fig. 2b): their average  $E_D = -5 \pm 1$  meV lies within the KI gap, and their distinct velocities,  $v_{\bar{X}} \approx 1,150 \pm 40$  m s<sup>-1</sup> and  $v_{\bar{\Gamma}} \approx 14,000 \pm 1,000$  m s<sup>-1</sup>, identify them as Dirac states positioned at the  $\bar{X}$  point and the  $\bar{\Gamma}$  point, respectively (Fig. 1d). The largest effective Dirac mass<sup>9</sup> is at the  $\bar{X}$  point with  $m^* = \hbar k_F / v_{D_{\bar{X}}} = (410 \pm 20) m_e$ . The size of each Fermi pocket ( $k_F$ ) along  $q_y$ , is in excellent agreement with ARPES measurements<sup>17,18</sup>. Meanwhile, the apparent discrepancies

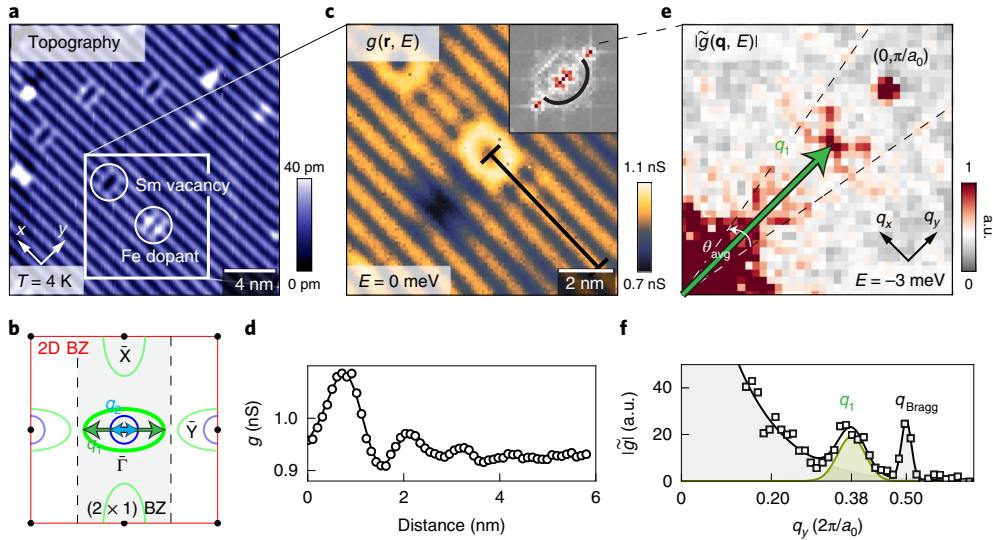


**Fig. 2 | Imaging QPI on the (2 × 1) surface of SmB<sub>6</sub>.** **a**, A (2 × 1) surface reconstruction on the half-Sm termination of SmB<sub>6</sub> doubles the unit cell in the *y* direction, creating the rows of atoms shown in the topographic image (sample bias  $V_s = -100$  mV, current set point  $I_s = 50$  pA). **b**, Correspondingly, the surface Brillouin zone is halved along  $k_y$ , folding the  $\bar{Y}$ -point Dirac cone to  $\bar{\Gamma}$ . **c**, Atomic defects on the surface scatter momentum eigenstates to generate QPI patterns in the spatially resolved differential conductance,  $g(\mathbf{r}, E = 0$  meV), measured in the boxed area in **a** ( $V_s = -100$  mV,  $I_s = 150$  pA). In this region, QPI appears as a ring in the Fourier transform (FT) of differential conductance,  $|\tilde{g}(\mathbf{q}, E)|$  (green line in inset). **d**, The QPI is short ranged around defects, reflecting contributions from localized *f* states; it decays after a few periods in this linecut along the black line in **c**. **e**, In a larger, 30-nm area, the QPI signal in  $|\tilde{g}(\mathbf{q}, E = -3$  meV) $|$  manifests as a broad peak with the highest signal to noise ratio along  $q_y$  ( $V_s = 30$  mV,  $I_s = 180$  pA). At this energy, it occurs at the  $q_y$  vector corresponding to intra-cone backscattering within the  $\bar{X}$ -point Dirac cone (labelled  $q_1$  in **b**). The image has been twofold symmetrized to increase signal to noise ratio. **f**, We quantified QPI peaks by fitting linecuts of  $|\tilde{g}(\mathbf{q}, E)|$  along  $q_y$ , averaged over an angle  $\theta_{\text{avg}} = 20^\circ$  to a sum of Gaussians that capture contributions from the Bragg peak ( $q_{\text{Bragg}}$ ), low- $\mathbf{q}$  disorder and dispersing QPI (green peak labelled  $q_1$ ).

between our measured velocities and Dirac points, and those of ARPES, can be explained by the fact that we access a single, non-polar surface, whereas ARPES experiments typically average over a mixture of terminations<sup>23</sup>.

Intracone backscattering, illustrated in Fig. 2b, is the simplest identifiable process responsible for the observed Dirac-state QPI. In this scenario, the QPI scattering vector is given by  $2\mathbf{k}(E)$ , and the experimentally derived  $\mathbf{k}_F$  is in good agreement with the size of surface state Fermi pockets in electronic structure calculations<sup>4</sup> (see Supplementary Section II). Yet, the observation of backscattering is unusual, because in the simplest model for topological surface states, whereby Dirac cones have an in-plane helical spin structure, neither magnetic nor non-magnetic backscattering leads to a peak in the QPI spectrum<sup>32</sup>. On the other hand, introducing even weak out-of-plane ferromagnetic correlations immediately restores the backscattering peak for magnetic defects, while preserving the Dirac cone structure (see Supplementary Section III). Such ferromagnetic canting can occur due to the Dzyaloshinskii–Moriya interaction, the local spin polarization induced by magnetic defects<sup>33</sup>, or in topological insulators with strong interactions, such as TKIs, where it was shown theoretically that surface states possess an out-of-plane spin polarization<sup>3,34</sup>. As it turns out, hysteresis associated with surface ferromagnetism was recently observed in SmB<sub>6</sub> at low temperature<sup>35</sup>. In addition, we found that a small inclusion of nominally non-magnetic Sm vacancies led to an enhanced magnetic susceptibility at low temperatures, akin to the addition of Kondo holes<sup>36</sup> (see also Supplementary Section III). In fact, the combination of magnetic defects and local ferromagnetic correlations was also proposed as the origin of the backscattering QPI signal recently measured in magnetically doped topological insulators<sup>37</sup>.

To associate the Dirac states detected from QPI with a TKI phase, we also tracked their temperature dependence in tunnelling spectra,  $g(E, T)$ . Unlike trivial surface states, the formation of

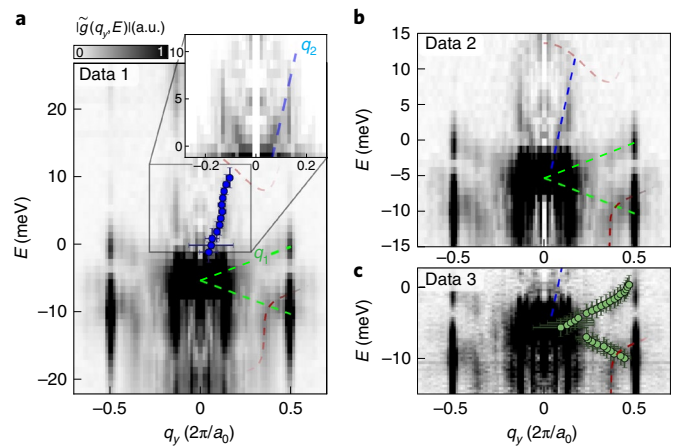


**Fig. 3 | Raw QPI reveals heavy Dirac surface states.** **a–c**, Angle-averaged linecuts along  $q_y$  of  $|\tilde{g}(q_y, E)|$  on three different sample areas give consistent results. In each case, dispersing QPI signals are marked by dashed guides: green (labelled  $q_1$ ) and blue ( $q_2$ ) lines track surface states, while the red guides track KI states. A box-windowed FT (magnified inset in **a**) enhances the low- $\mathbf{q}$  signal (blue) compared with the Hanning-windowed FT that reduces spread of the high- $\mathbf{q}$  states in the main panel. The  $q$ -axis error bars are estimates based on the covariance matrix of the Gaussian fits, whereas the  $E$ -axis error bars show the energy resolution of the STM. Data in **a, c** were acquired under  $B = 0$  T, and **b** has  $B = 9$  T, which does not noticeably affect the QPI. All other data acquisition parameters are listed in Supplementary Table 1.

heavy Dirac fermions at the surface of a TKI is predicated on the coherence of the correlation-driven KI gap. With increasing temperature, incoherent Kondo lattice states spread into this gap as the

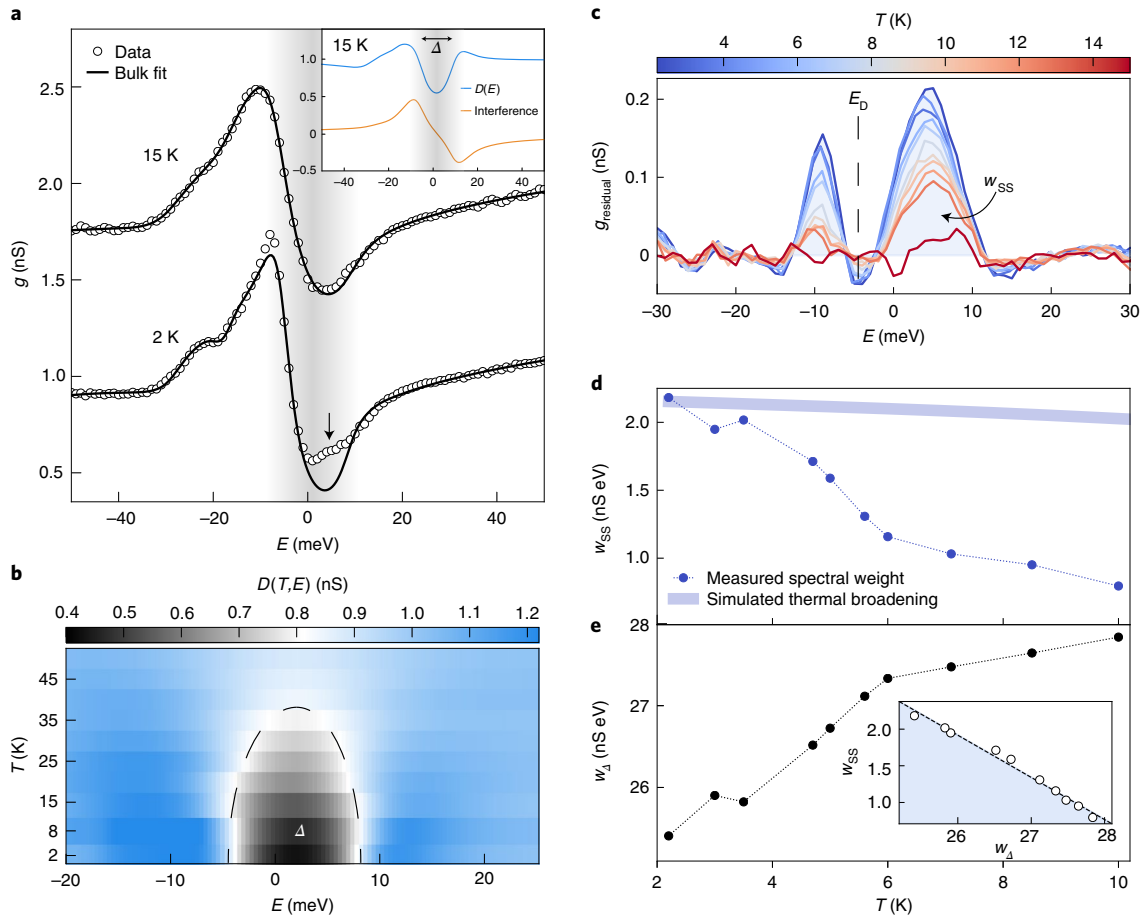


**Fig. 4 | Concomitant evolution of Dirac states and the KI gap.** **a**, Quantum mechanical interference of electrons tunnelling from the tip to either *d* or *f* states in the  $\text{SmB}_6$  Kondo lattice leads to a characteristic peak-dip lineshape in  $g(E)$  data (open circles). At 15 K, the data is well described by a cotunnelling model (equation (1), black line), allowing bulk KI state contributions ( $D(E)$ , blue line in inset) to be disentangled from interference effects (orange). Yet at 2 K, the fit deviates for energies within the KI gap (grey region), signalling the onset of an additional conductance channel (surface states, arrow) not captured in our bulk KI model. **b**, The temperature evolution of KI states,  $D(E)$ , from fitting  $g(E, T)$  to a co-tunnelling model (see blue curve in **a**).  $\Delta$  appears below  $T_\Delta \approx 35$  K and reaches  $\Delta \approx 14$  meV at 2 K. **c**, The deviations of  $g(E)$  from the co-tunnelling model intensify with lowering temperature. They are characteristic of a linear band dispersion with a nodal energy of  $E_D = -5$  meV, and match our independent raw QPI measurements of Dirac surface states (see Fig. 3). **d**, The rapid onset of the Dirac surface states, captured from integrating the fit residuals in **c** ( $w_{SS}$ , blue dots), cannot be explained by thermal broadening (thick blue line, see Supplementary Section X). **e**, Instead, it is correlated with the development of the bulk KI gap, calculated by integrating  $D(E)$  for energies within  $\Delta$  to find the in-gap spectral weight  $w_d$ , demonstrating the direct relationship between the evolving host insulator and its topologically emergent states (see inset).

hybridization between *f* and *d* electrons unwinds. Eventually, this process is expected to drive a topological phase transition as band-parity inversion is lost, eliminating the non-trivial surface states. However, theory has not yet succeeded in describing coherent Kondo lattice evolution, much less the concomitant formation of heavy Dirac fermions. Here, we experimentally extract this complex connection by tracking the simultaneous temperature evolution of the KI gap and Dirac surface state contributions to  $g(E)$ . In general,  $g(E)$  cannot be directly interpreted as the density of states in multi-orbital Kondo lattice systems due to the quantum interference between electrons co-tunnelling into *f* and *d* states<sup>38,39</sup>. We account for this effect by modelling the differential conductance spectrum as

$$g(\mathbf{r}_0, E) \propto [\mathbf{t}^T \text{Im}G(\mathbf{r} - \mathbf{r}_0 = 0, E)t], \quad \mathbf{t}^T = [t_d \ t_{f_1} \ t_{f_2}], \quad (1)$$

where  $\mathbf{t}$  is a vector of the tunnelling probability for each orbital and  $G(\mathbf{r}, E)$  is the Fourier transform of  $\tilde{G}(\mathbf{k}, E)$ , the renormalized KI Green's function describing a tight-binding Hamiltonian that

qualitatively reproduces known bulk bands<sup>4</sup> (see also Supplementary Section IX). Equation (1) includes contributions only from the underlying KI, but not from emergent topological surface states. Even so, it accurately captures all features in  $g(E)$  at 15 K (Fig. 4a), implying that surface states are negligible at this temperature. Fits to equation (1) can be further decomposed into interference terms and the bulk density of states,  $D(E)$ , weighted by the relative tunnelling probabilities (Fig. 4a inset). As temperature is lowered,  $D(E, T)$  exhibits a narrow energy window of diminished spectral weight that onsets below  $T_\Delta \approx 35$  K and expands to  $\Delta \approx 14$  meV at low temperatures (Fig. 4b), in correspondence with bulk measurements of the KI gap in  $\text{SmB}_6$  (refs. 10–13).

The heavy Dirac surface states in  $\text{SmB}_6$  emerge only at low temperatures as the KI gap becomes coherent. They are visible in our measurements of  $g(E)$  at 2 K as an additional contribution within the KI gap that is not captured by equation (1) (see arrow in Fig. 4a). The differences between  $g(E)$  and fits to equation (1) are characteristic of linear bands with a crossing point near  $-5$  meV (Fig. 4c), which perfectly matches our independent QPI measurements of

heavy Dirac surface states (Fig. 3). Similar temperature-dependent features in  $g(E)$  spectra have also been observed on the  $(1 \times 1)$  boron termination<sup>31</sup>. We quantified the emergence of the surface states by integrating  $g_{\text{residual}}(E)$  at each temperature (Fig. 4d). We found that the surface states diminish rapidly with increasing temperature, faster than can be accounted for by thermal broadening alone (blue line in Fig. 4d), and indeed faster even than the filling of the insulating gap at around 35 K where the topology of the bands is inverted (see also Supplementary Section X). One possible explanation for this fast decay is that the surface states are reliant on bulk coherence. Certainly, the evolution of their spectral weight is correlated with the weight of residual states in the KI gap, calculated by integrating  $D(E)$  for energies within  $\Delta$  (Fig. 4e). Alternatively, the unusually fast decay of the surface states may reflect their interactions with magnetic correlations generated by Kondo lattice defects<sup>31,40</sup>.

Our simultaneous imaging of Kondo insulator formation and slow in-gap surface modes is consistent with  $\text{SmB}_6$  hosting a correlation-driven topological surface state that harbours the heaviest known Dirac fermions. The optimal positioning of the  $f$ -character surface states at the chemical potential, enforced by Kondo lattice interactions, increases prospects for interface engineering to discover novel forms of topological superconductivity and construct transformative quantum devices.  $\text{SmB}_6$  and prospective TKIs may become leading testbeds for fractional and non-Abelian statistics, both of which are essential elements of prospective universal topological quantum computation.

### Online content

Any methods, additional references, Nature Research reporting summaries, source data, extended data, supplementary information, acknowledgements, peer review information; details of author contributions and competing interests; and statements of data and code availability are available at <https://doi.org/10.1038/s41567-019-0700-8>.

Received: 6 December 2018; Accepted: 19 September 2019;

Published online: 11 November 2019

### References

- Dzero, M., Sun, K., Galitski, V. & Coleman, P. Topological Kondo insulators. *Phys. Rev. Lett.* **104**, 106408 (2010).
- Alexandrov, V., Dzero, M. & Coleman, P. Cubic topological Kondo insulators. *Phys. Rev. Lett.* **111**, 226403 (2013).
- Takimoto, T.  $\text{SmB}_6$ : a promising candidate for a topological insulator. *J. Phys. Soc. Jpn* **80**, 123710 (2011).
- Lu, F., Zhao, J., Weng, H., Fang, Z. & Dai, X. Correlated topological insulators with mixed valence. *Phys. Rev. Lett.* **110**, 096401 (2013).
- Efimkin, D. K. & Galitski, V. Strongly interacting Dirac liquid on the surface of a topological Kondo insulator. *Phys. Rev. B* **90**, 081113 (2014).
- Wang, C., Potter, A. C. & Senthil, T. Gapped symmetry preserving surface state for the electron topological insulator. *Phys. Rev. B* **88**, 115137 (2013).
- Chen, X., Fidkowski, L. & Vishwanath, A. Symmetry enforced non-Abelian topological order at the surface of a topological insulator. *Phys. Rev. B* **89**, 165132 (2014).
- Thomson, A. & Sachdev, S. Fractionalized Fermi liquid on the surface of a topological Kondo insulator. *Phys. Rev. B* **93**, 125103 (2016).
- Dzero, M., Xia, J., Galitski, V. & Coleman, P. Topological Kondo insulators. *Annu. Rev. Condens. Matter Phys.* **7**, 249–280 (2016).
- Allen, J. W., Batlogg, B. & Wachter, P. Large low-temperature Hall effect and resistivity in mixed-valent  $\text{SmB}_6$ . *Phys. Rev. B* **20**, 4807–4813 (1979).
- Kim, D. J., Xia, J. & Fisk, Z. Topological surface state in the Kondo insulator samarium hexaboride. *Nat. Mater.* **13**, 466–470 (2014).
- Zhang, X. et al. Hybridization, inter-ion correlation, and surface states in the Kondo insulator  $\text{SmB}_6$ . *Phys. Rev. X* **3**, 011011 (2013).
- Syers, P., Kim, D., Fuhrer, M. S. & Paglione, J. Tuning bulk and surface conduction in the proposed topological Kondo insulator  $\text{SmB}_6$ . *Phys. Rev. Lett.* **114**, 096601 (2015).
- Luo, Y., Chen, H., Dai, J., Xu, Z.-A. & Thompson, J. D. Heavy surface state in a possible topological Kondo insulator: magnetothermoelectric transport on the (011) plane of  $\text{SmB}_6$ . *Phys. Rev. B* **91**, 075130 (2015).
- Li, G. et al. Two-dimensional Fermi surfaces in Kondo insulator  $\text{SmB}_6$ . *Science* **346**, 1208–1212 (2014).
- Tan, B. S. et al. Unconventional Fermi surface in an insulating state. *Science* **349**, 287–290 (2015).
- Xu, N. et al. Exotic Kondo crossover in a wide temperature region in the topological Kondo insulator  $\text{SmB}_6$  revealed by high-resolution ARPES. *Phys. Rev. B* **90**, 085148 (2014).
- Jiang, J. et al. Observation of possible topological in-gap surface states in the Kondo insulator  $\text{SmB}_6$  by photoemission. *Nat. Commun.* **4**, 3010 (2013).
- Neupane, M. et al. Surface electronic structure of the topological Kondo-insulator candidate correlated electron system  $\text{SmB}_6$ . *Nat. Commun.* **4**, 2991 (2013).
- Gorshunov, B. et al. Low-energy electrodynamics of  $\text{SmB}_6$ . *Phys. Rev. B* **59**, 1808–1814 (1999).
- Frantzeskakis, E. et al. Kondo Hybridization and the origin of metallic states at the (001) surface of  $\text{SmB}_6$ . *Phys. Rev. X* **3**, 041024 (2013).
- Hlawenka, P. et al. Samarium hexaboride is a trivial surface conductor. *Nat. Commun.* **9**, 517 (2018).
- Matt, C. E. et al. Consistency between ARPES and STM measurements on  $\text{SmB}_6$ . Preprint at <http://arxiv.org/abs/1810.13442> (2018).
- Ruan, W. et al. Emergence of a coherent in-gap state in the  $\text{SmB}_6$  Kondo insulator revealed by scanning tunneling spectroscopy. *Phys. Rev. Lett.* **112**, 136401 (2014).
- Rößler, S. et al. Hybridization gap and Fano resonance in  $\text{SmB}_6$ . *Proc. Natl Acad. Sci. USA* **111**, 4798–4802 (2014).
- Zhu, Z.-H. et al. Polarity-driven surface metallicity in  $\text{SmB}_6$ . *Phys. Rev. Lett.* **111**, 216402 (2013).
- Strosio, J. A., Feenstra, R. M. & Fein, A. P. Electronic structure of the  $\text{Si}(111)2 \times 1$  surface by scanning-tunneling microscopy. *Phys. Rev. Lett.* **57**, 2579–2582 (1986).
- Schmidt, A. R. et al. Imaging the Fano lattice to ‘hidden order’ transition in  $\text{URu}_2\text{Si}_2$ . *Nature* **465**, 570–576 (2010).
- Aynajian, P. et al. Visualizing heavy fermions emerging in a quantum critical Kondo lattice. *Nature* **486**, 201–206 (2012).
- Allan, M. P. et al. Imaging cooper pairing of heavy fermions in  $\text{CeCoIn}_5$ . *Nat. Phys.* **9**, 468–473 (2013).
- Jiao, L. et al. Additional energy scale in  $\text{SmB}_6$  at low-temperature. *Nat. Commun.* **7**, 13762 (2016).
- Guo, H.-M. & Franz, M. Theory of quasiparticle interference on the surface of a strong topological insulator. *Phys. Rev. B* **81**, 041102 (2010).
- Nyberg, R. H., Rossi, E. & Morr, D. K. Identifying collective modes through impurity pinning in cuprate superconductors. *Phys. Rev. B* **78**, 054504 (2008).
- Baum, Y. & Stern, A. Magnetic instability on the surface of topological insulators. *Phys. Rev. B* **85**, 121105 (2012).
- Nakajima, Y., Syers, P., Wang, X., Wang, R. & Paglione, J. One-dimensional edge state transport in a topological Kondo insulator. *Nat. Phys.* **12**, 213–217 (2015).
- Figgins, J. & Morr, D. K. Defects in heavy-fermion materials: unveiling strong correlations in real space. *Phys. Rev. Lett.* **107**, 066401 (2011).
- Okada, Y. et al. Direct observation of broken time-reversal symmetry on the surface of a magnetically doped topological insulator. *Phys. Rev. Lett.* **106**, 206805 (2011).
- Maltseva, M., Dzero, M. & Coleman, P. Electron cotunneling into a Kondo lattice. *Phys. Rev. Lett.* **103**, 206402 (2009).
- Figgins, J. & Morr, D. K. Differential conductance and quantum interference in Kondo systems. *Phys. Rev. Lett.* **104**, 187202 (2010).
- Akintola, K. et al. Quantum spin fluctuations in the bulk insulating state of pure and Fe-doped  $\text{SmB}_6$ . *Phys. Rev. B* **95**, 245107 (2017).

**Publisher's note** Springer Nature remains neutral with regard to jurisdictional claims in published maps and institutional affiliations.

© The Author(s), under exclusive licence to Springer Nature Limited 2019

## Methods

STM experiments were carried out on single crystals of pure, 0.1% Gd-doped and 0.5% Fe-doped  $\text{SmB}_6$  grown using the Al-flux method<sup>41</sup>. Crystals were cleaved in a cryogenic ultrahigh vacuum at ~30 K and immediately inserted into our home-built STM. STM tips were cut from PtIr wire and cleaned by in situ field emission on Au foil. The cryogenic ultrahigh vacuum environment allowed the cleaved surface to stay clean for several months. Data were collected on three different samples and multiple fields of view.

Magnetic susceptibility measurements were performed on single-crystalline samples of  $\text{SmB}_6$  and  $\text{Sm}_{0.95}\text{B}_6$  grown by the Al-flux technique with starting composition  $\text{Sm}:\text{B}:\text{Al} = 1 - x:6:700$  ( $x = 0.0$  and  $0.05$ , respectively). The mixture of samarium pieces, boron powder (99.99%) and aluminium shots (99.999%) was placed in an alumina crucible and loaded in a vertical tube furnace with ultrahigh-purity Ar flow. The furnace was heated to 1,723 K for 12 h followed by slow cooling to 1,323 K at  $2^\circ\text{C h}^{-1}$ . At 1,323 K the furnace was shut down, and the flux was removed at room temperature by etching with a NaOH solution. The atomic structure of the resulting single crystals was verified by X-ray diffraction at room temperature in a Bruker D8 Venture diffractometer using a Mo K $\alpha$  X-ray source. A Quantum Design superconducting quantum interference device was used to measure the magnetic response of the crystals to a magnetic field of 1 kOe. The magnetic susceptibility curves were normalized to their values at 350 K because of the uncertainty in the determination of the actual number of Sm vacancies.

## Data availability

The data that support the findings of this study are available from the corresponding author on reasonable request.

## Code availability

The code that supports the findings of this study is available from the corresponding author on reasonable request.

## References

41. Kim, D. J. et al. Surface Hall effect and nonlocal transport in  $\text{SmB}_6$ : evidence for surface conduction. *Sci. Rep.* **3**, 3150 (2013).

## Acknowledgements

The work at Harvard was supported by the US National Science Foundation under grant nos. DMR-1106023 and DMR-1410480. The work at UC Irvine was supported by US National Science Foundation under grant no. 1708199. D.K.M. acknowledges support by the US Department of Energy, Office of Science, Basic Energy Sciences, under award no. DE-FG02-05ER46225. Work at Los Alamos was supported by the US Department of Energy, Office of Basic Energy Sciences, Division of Materials Science and Engineering. Work at the University of Maryland was funded by AFOSR grant no. FA9550-14-1-0332 and by the Gordon and Betty Moore Foundation's EPiQS Initiative through grant no. GBMF4419.

## Author contributions

H.P., Y.L., A.S., P.C., Y.H. and M.M.Y. performed the STM experiments. X.W., J.P., P.F.S.R., D.J.-K. and Z.F. synthesized and characterized the samples. P.F.S.R. performed X-ray measurements. J.D.T. performed magnetic susceptibility measurements. H.P., A.S., Y.H., M.M.Y., M.H.H. and J.E.H. developed and carried out analyses. D.K.M. provided theoretical guidance. M.H.H. and J.E.H. supervised the project. H.P. and M.H.H. wrote the paper with key contributions from D.K.M. and J.E.H. The manuscript reflects the contributions and ideas of all authors.

## Competing interests

The authors declare no competing interests.

## Additional information

**Supplementary information** is available for this paper at <https://doi.org/10.1038/s41567-019-0700-8>.

**Correspondence and requests for materials** should be addressed to M.H.H. or J.E.H.

**Reprints and permissions information** is available at [www.nature.com/reprints](http://www.nature.com/reprints).